Internal Plasma Structure Measurements of a Hall Thruster Using Xenon and Krypton Propellant

IEPC-2005-024

Presented at the 29th International Electric Propulsion Conference, Princeton University, October 31 – November 4, 2005

Jesse A. Linnell* and Alec D. Gallimore†
Plasmadynamics and Electric Propulsion Laboratory, Department of Aerospace Engineering, University of Michigan, Ann Arbor, MI 48109 USA

For krypton to become a realistic option for Hall thruster operation it is necessary to understand the performance gap between xenon and krypton and what can be done to reduce it. A floating emissive probe is used with the Plasmadynamics and Electric Propulsion Laboratory's High-speed Axial Reciprocating Probe system to map the internal plasma potential structure of the NASA-173Mv1 Hall thruster using xenon and krypton propellant. Measurements are taken for both propellants at discharge voltages of 500 and 600 V and discharge currents of 9.27 and 9.59 A, respectively. Electron temperature and electric field are also calculated and reported. The acceleration zone and equipotential lines are found to be strongly linked to the magnetic field lines. The plasma lens effect of the NASA-173Mv1 Hall thruster strongly focuses the xenon ions toward the center of the discharge channel whereas the krypton ions are defocused. Krypton is also found to have a longer acceleration zone than the xenon cases. These results explain the large beam divergence observed with krypton operation. Krypton and xenon have similar maximum electron temperatures and similar lengths of the high electron temperature zone, although the high electron temperature zone is located farther downstream in the krypton case.

I. Introduction

Hall thrusters[1,2] are space propulsion devices that use crossed electric and magnetic fields to ionize and accelerate propellant atoms to high exhaust velocities. The electric field is established by an electron current that crosses and is concurrently impeded by the magnetic field. The magnetic field causes the electrons to follow a closed drift path and for this reason Hall thrusters are often referred to as closed drift thrusters. Noble gases of high atomic weight, such as xenon and krypton, are the most common choice of propellant.

Due to the relative high price and scarcity of xenon and the superior specific impulse of krypton, krypton has recently sparked interest in the electric propulsion community. Even for small scale missions, the financial savings in propellant cost alone can be tens of thousands of dollars given krypton's high specific impulse and low price. Although previous studies[3-7] report krypton to have an inferior performance as compared to xenon, recent results using the NASA-457M[8] and the NASA-400M[9] indicate that krypton can be operated at efficiencies comparable to xenon. Before krypton can become a legitimate option for space propulsion, the reasons for the krypton efficiency gap must be fully understood and the efficiency gap must be reduced.

Previous researchers[4,5,9] have consistently concluded that the dominant contributing factor to krypton's inferior efficiency is propellant utilization. It has recently been shown that beam divergence is also a significant contributor

* Ph.D. Candidate, Aerospace Engineering, jlinnell@umich.edu.
† Professor and Laboratory Director, Aerospace Engineering, alec.gallimore@umich.edu.

to krypton-xenon efficiency gap.[10] To obtain a greater understanding of the krypton-xenon efficiency gap, it will be necessary to collect information about the plasma behavior internal to the Hall thruster discharge channel.

Internal floating emissive probe measurements have been conducted for the NASA-173Mv1 operating with xenon and krypton and are reported in the following paper. The floating emissive probe is mounted on the Plasmadynamics and Electric Propulsion Laboratory (PEPL) High-Speed Axial Reciprocating Probe (HARP) system and the emissive probe is sweep into the thruster discharge channel. This provides an internal mapping of the plasma potential structure. Similar methods of characterizing the internal potential structure of Hall thrusters has been used by other researchers.[11-17] In addition to the plasma potential, the electron temperature and electric field are also extracted from the data. For both krypton and xenon, the Hall thruster is operated at discharge voltage of 500 and 600 V with a corresponding discharge current of 9.27 and 9.59 A, respectively. High-voltage operation is chosen because krypton Hall thrusters would most likely be designed for high-voltage operation in order to benefit from on krypton's superior specific impulse.

II. Experimental Setup and Apparatus

A. Facility

The measurements reported in this paper were conducted in the Large Vacuum Test Facility (LVTF) at PEPL. The LVTF is a cylindrical stainless-steel tank that is 9 m long and 6 m in diameter. The vacuum chamber is evacuated using seven CVI model TM-1200 internal cryopumps, which combined are capable of pumping 240,000 l/s of xenon and 252,000 l/s of krypton. The vacuum tank pressure is monitored by using two hot-cathode ionization gauges. The vacuum chamber operates at a base pressure of 1.5×10^{-7} Torr and approximately 3.3×10^{-6} Torr (corrected[18]) during all thruster operating points.

High-purity research grade xenon and krypton are used as propellants for the following measurements. The purity level of xenon and krypton are 99.9995% and 99.999%, respectively. The propellants are supplied through propellant feel lines using 20 and 200 sccm mass flow controllers for the cathode and anode, respectively. The mass flow controllers are calibrated using a constant volume method. The compressibility correction factor is calculated using the van der Waals Equation[19] and the Virial Equation.[20] Error in the mass flow controllers is approximately ±1% of full scale.

B. Experimental Setup

As shown in Fig. 1, the NASA-173Mv1 is mounted on two linear (radial and axial) tables that control the probe alignment and positioning. The emissive probe is mounted on the HARP system, which is securely fixed downstream of the thruster to dampen any vibrations caused by the high acceleration of the probe. These individual components are discussed in greater detail below.

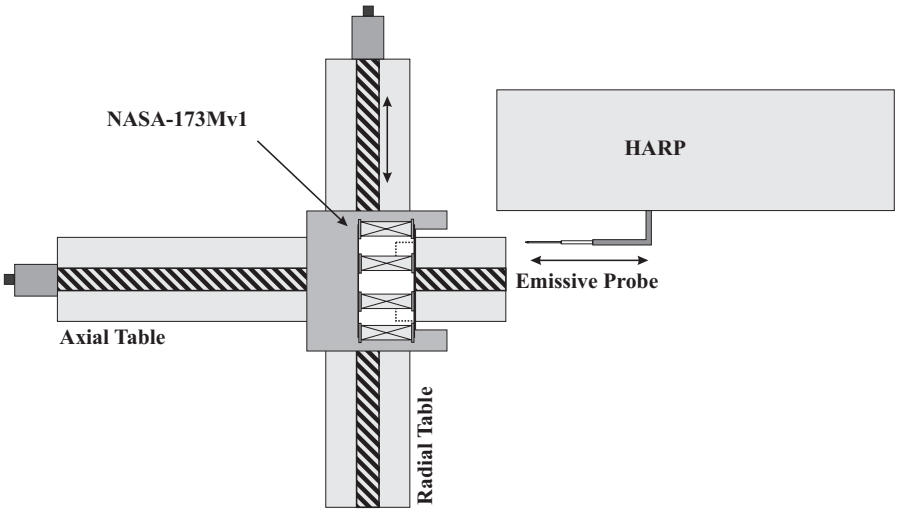

Figure 1. Internal Floating Emissive Probe Experimental Setup

C. Thruster

The NASA-173Mv1 Hall thruster[21] (Fig. 2) is used for all measurements. In addition to the standard inner and outer magnetic coils, the NASA-173Mv1 uses a trim coil to shape the magnetic field topology. The thruster is run for one hour for the initial conditioning and is warmed up for at least 30 minutes at a given operation point before data are taken.

The magnetic field created by the trim coil is found to improve thruster efficiency by establishing what is commonly referred to as a plasma lens.[1,21-25] A plasma lens uses magnetic field lines with a curvature that focus ions toward the center of the discharge channel.[17] This can be explained because to first order the magnetic field lines chart the equipotential lines inside a Hall thruster.[26] In addition to improved beam focusing, this magnetic field topology has also been shown to improve ion acceleration processes and internal electron dynamics.[10,21]

A Busek BHC-50-3UM hallow cathode is used for all measurements. The cathode flow rate is equal to 10% of the anode flow rate. The cathode axial centerline is mounted 30 degrees off horizontal and the center of the cathode orifice is placed 30 mm downstream and 30 mm above the thruster outer face.

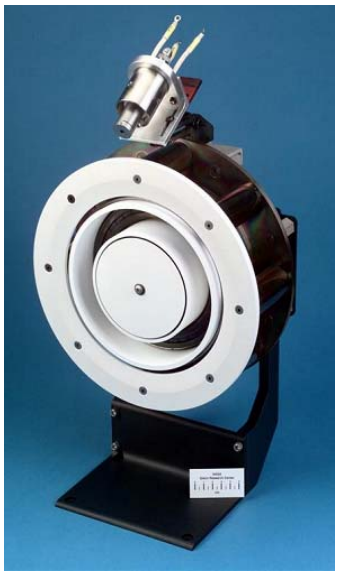

Figure 2. NASA-173Mv1 Hall Thruster

D. High-Speed Axial Reciprocating Probe

The HARP[27,28] (Fig. 3) has a linear motor assembly providing direct linear motion at very high speed and large acceleration. The linear motor is an LM210 manufactured by Trilogy that has a three-phase brushless DC servomotor consisting of a linear, "U"-shaped magnetic track and a "T"-shaped coil moving on a set of linear tracks. A linear encoder provides positioning resolution to 5 microns. The table is covered by a stainless steel and graphite shroud to protect the HARP from excessive heating and high-energy ions. One side has a thin slit running the length of the table through which a probe boom extends. The HARP is capable of moving small probes at speeds of 250 cm/s with linear accelerations of 7 g's. For this experiment, the probe is swept at 150 cm/s and residence time inside the discharge channel is kept under 80 ms.

Figure 3. High-Speed Axial Reciprocating Probe System

E. Emissive Probe

1. Probe Description

The emissive probe design is based on the work done by Haas at PEPL.[11] The emissive probe is composed of 1.5-mm-diameter double bore alumina insulator. The emitting filament is 1% thoriated tungsten with a diameter of 0.0127 cm. The electrical connection along the length of the probe is completed using 30 AWG copper leads that are slightly recessed into the alumina shaft. Additional short lengths of thoriated tungsten wire are inserted into the alumina tubing to provide a tight fit and guarantee good contact between the emitter and copper wires. A schematic of the emissive probe design appears in Fig. 4.

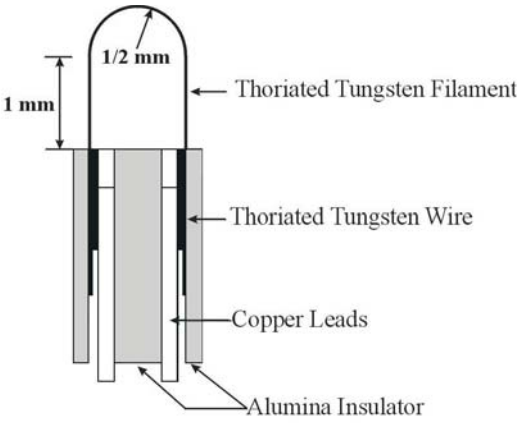

Figure 4. Emissive Probe Schematic

The diameter of the emitting filament (0.0127 cm)

is much smaller than the electron gyroradius inside the Hall thruster. This condition is necessary for unmagnetized probe theory to be valid.[29] The filament size used in these measurements is of the same emitter diameter used by Haas[11] and similar to the emitter diameter used by Raitses et al.[13-16,30,31]

The area mapped by the emissive probes is displayed in Fig. 5. The origin is taken to be the location where the inner wall meets the anode. Five axial sweeps spaced 5 mm apart are taken inside the Hall thruster discharge channel. The probe is aligned so that the filament tip travels from 137 mm to within 10 mm of the anode. However, in order to accentuate the areas of interest, the results section only shows the emissive probe findings in the region from 0 to 100 mm. The emissive probe is positioned so that the plane of the filament loop is normal to the thruster radial direction. The expected resolution of the emissive probe is 1.5 mm, which is the approximate size of the filament loop.

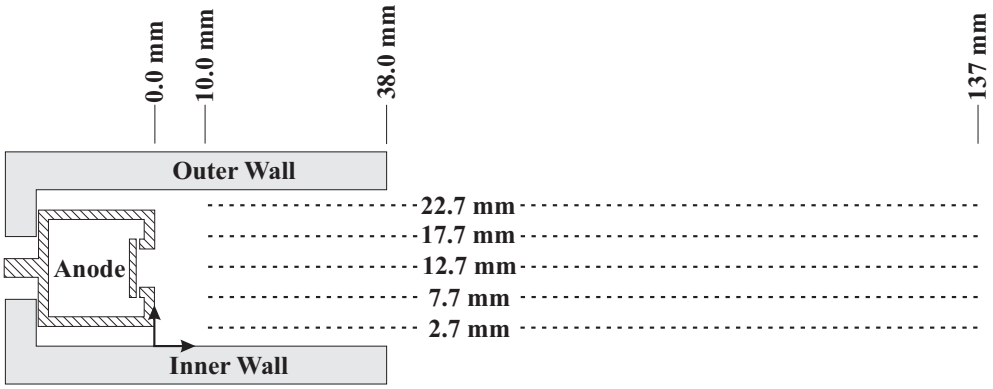

Figure 5. The Emissive Probe Mapping Region

The floating emissive probe circuit consists of the emissive probe, an isolation amplifier, and a floating power supply capable of supplying enough current to heat the filament (3-4 A). The floating emissive probe circuit is shown in Fig. 6. The sampling rate of the oscilloscope is dictated by the transit speed of the probe and is set to sample every 0.5 mm. This sampling speed is sufficient to easily capture the 1.5 mm resolution dictated by the probe dimensions. This sampling rate results in aliasing of the signal so that high frequency oscillations in the 10-30 kHz range, typical of the Hall thruster breathing mode, cannot be resolved. Therefore, the data presented constitute "time-averaged" measurements. The probe position and the perturbations to the discharge current and cathode potential are also recorded by the oscilloscope. During post processing, a gentle spline smoothing[32] is used to reduce the signal noise from the probe position, and floating probe potential. Examples of a typical data sweep are given in Fig. 7, which shows the floating potential and the perturbations to the thruster as the probe is swept into the discharge channel. In this figure V_p is the plasma potential, V_k is the cathode potential and I_D is the discharge current. For the reported data the perturbations to the discharge current are below 15-20%.

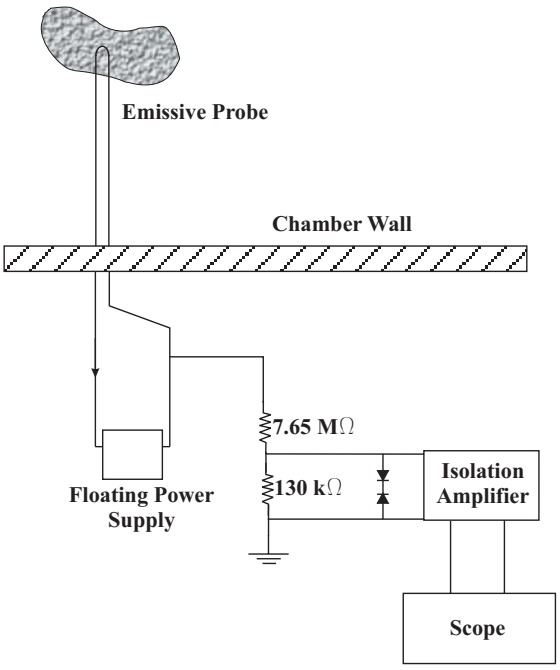

Figure 6. Floating Emissive Probe Circuit

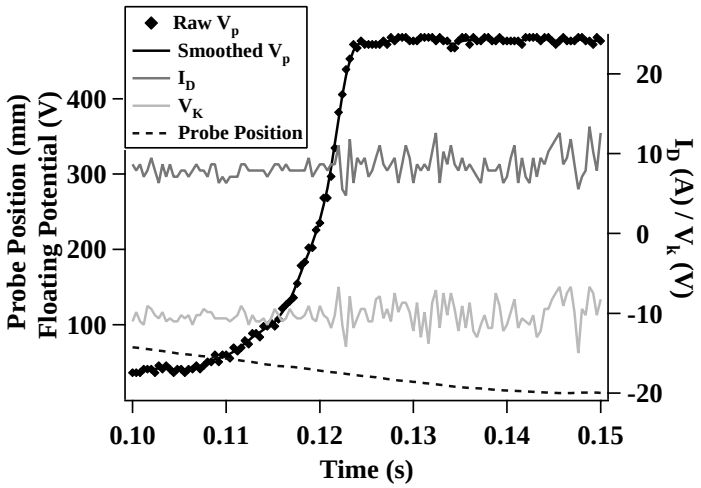

Figure 7. Emissive Probe Sweep Example

2. Space Charge Limited Sheath Correction

Space charge effects must be taken into account when analyzing emissive probe data in Hall thrusters. The space charge limit is reached when the emitted electron current to collected electron current ratio (δ) reaches a critical ratio (δ_c) that is approximately equal to one. Hobbs and Wesson[33] present an equation for critical emission: δ_c=1-8.3$(m_e/M_i)^{1/2}$. In this equation, of electron mass is given by m_e and ion mass is given by M_i. As δ approaches δ_c, the electric field at the probe surface decreases and tends toward zero. Once δ becomes greater than δ_c, a potential well forms and emitted electrons are returned to the probe, creating a double sheath.

The space charge limited sheath surrounding the emissive probe appears in Fig. 8. For the following discussion, the probe sheath is separated into 2 sections: The collector sheath and presheath. Three lines representing possible collector sheaths appear in Fig. 8: i) $\delta < \delta_c$, insufficiency electron emission; ii) $\delta=\delta_c \approx 1$, space charge limited regime; and iii) $\delta >> 1$, very strong electron emission.[34] Due to the extremely frailty of the emissive probe inside the harsh Hall thruster discharge channel environment, the heater current is increased slowly until adequate filament heating is reached. Adequate heating is reached when the plasma potential profile no longer changes with increased electron emission. This heating method ensures that the probe is operating in the space charge limited regime (regime ii). Regime iii shown in Fig. 7 is an extreme case that will not occur before probe failure.

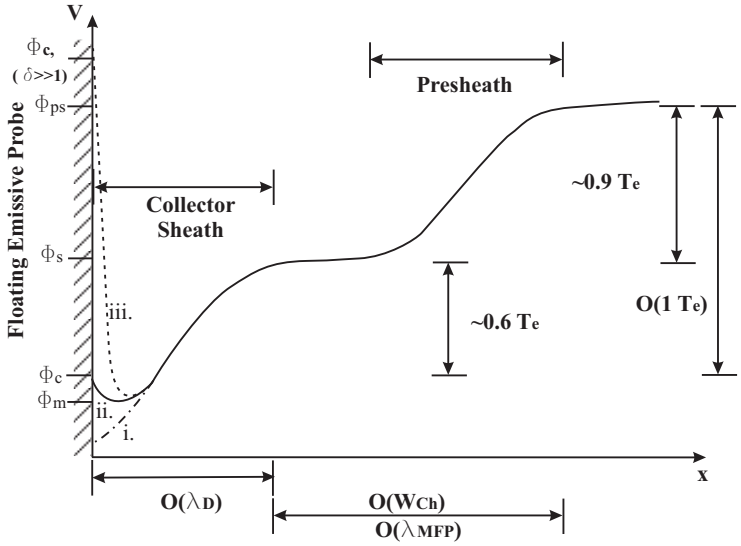

Figure 8. Emissive Probe Sheath. *The different operation regimes are shown by dashed lines and are labeled accordingly. (Not to scale)*

As a result of this space charge limited sheath, there is insufficient emitted electron current and the probe floats below the true plasma potential. The following correction[17] is applied to account for the space charge limited sheath.

The measured plasma potential is augmented by adding the collector sheath potential drop (0.6 T_e).[33,35] This will give the instantaneous plasma potential local to the emissive probe while avoiding added complication from trying to correct for the large presheath. The collector sheath size (~O(λ_D)) internal to the Hall thruster is on the same order as the wire diameter, which is an order of magnitude smaller than the total emitting tip dimensions and therefore the desired resolution of approximately 1.5 mm is maintained. Because of the presheath size is on the same order as the discharge channel width (W_{ch}),[36] it is difficult to account for the presheath potential drop while maintaining a meaningful spatial resolution. The potential drop (0.9 T_e)[35] across the presheath is considered a perturbation to the plasma and is used to define error bars for the measurement. In addition to the presheath perturbation, one half of the potential drop across the floating heater power supply should also be included in the error. The heater filament potential drop is 4 V. The total error associated with the plasma potential measurements is equal to ±0.9 T_e-2V.

3. Electron Temperature and Electric Field Calculation

Electron temperature can be calculated by using both "hot" and "cold" probe measurements.[12] Cold measurements refer to measurements taken with no filament heating. Equation 1 uses the potential drop across the collector sheath to calculate the electron temperature. In this equation, k_B is the Boltzmann constant, T_e is the electron temperature, V_f is the cold probe floating potential, and e is the electron charge. The error in this temperature calculation is ±17%.[13]

$$V_p - V_f = \frac{k_B T_e}{2e} \ln\left(\frac{M_i}{2\pi m_e}\right) \tag{1}$$

Axial and radial electric fields at each location inside the thruster are also presented below. A central difference method is used with the plasma potential to calculate the electric field. The forward difference technique is used for the first point, and backward difference approach for the last point.

III. Results and Discussion

The Hall thruster operating conditions for the internal emissive probe measurements are given in Table 1. Measurements are taken with xenon at discharge voltages of 500 and 600 V and an anode flow rate of 10 mg/s. Corresponding krypton points are taken that match the power levels of the xenon points. For each operation point, performance was optimized by monitoring thrust and thruster operating conditions to calculate real-time efficiencies. The magnet settings were varied and the *true* maximum efficiency for each operation point was found previous to this experiment. Therefore, each operation point has it own unique and optimized magnet settings.

For each operating condition the plasma potential, the electron temperature, axial electric field, and radial electric field are given. In the following maps, the magnetic field topology pathlines are overlaid with the plasma potential. The magnetic fields have been calculated using the 3D magnetostatic solver Magnet 6.0 by Infolytic.

Table 1. Thruster Operating Conditions

Point #	Propellant	V_k, V	V_d, V	I_d, A	Anode Flow, mg/s	Cathode Flow, mg/s	Inner Coil, A	Outer Coil, A	Trim Coil, A	Anode Effic., %
1	Xenon	-11.7	500	9.27	10.00	1.00	2.90	2.87	-0.87	66.1
2	Xenon	-12.3	600	9.59	10.00	1.00	3.17	3.42	-1.08	63.8
3	Krypton	-14.4	500	9.27	7.77	0.78	1.79	2.27	-0.43	56.6
4	Krypton	-13.3	600	9.59	7.80	0.78	1.98	2.18	-0.46	54.9

A. 500V Comparison

The internal plasma potential map for xenon and krypton at 500 V is shown in Fig. 9. These cases show a strong correlation between the magnetic field lines and the plasma potential. The xenon case displays a strong focusing in the equipotential lines that is due to the focusing effect of the magnetic lens. This behavior is also demonstrated computationally by Keidar.[37] However, the krypton equipotential lines have a less concave shape and are actually defocusing. This result is expected because krypton has been shown to have a larger beam divergence than xenon.[10] The differences in the shape of xenon and krypton equipotential lines are strongly related to their different magnetic

field topologies. Krypton operation requires lower magnet currents to achieve optimum efficiency and utilizes a weaker plasma lens. Efficiency optimization for the krypton data points are strongly connected to the propellant utilization optimization.[10] With propellant utilization being such an important focus of optimization, other efficiency components (such as beam divergence) suffer.

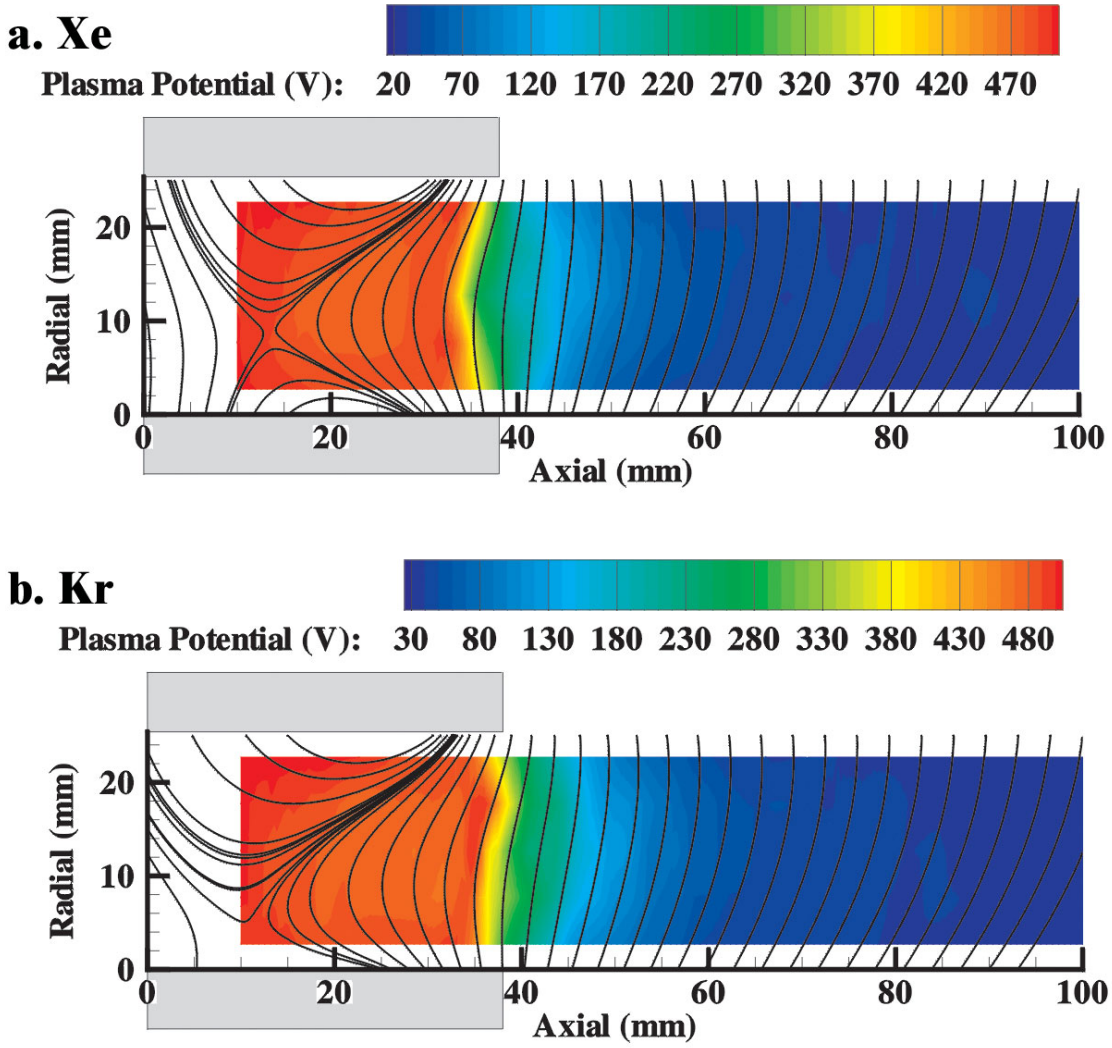

Figure 9. Plasma Potential Map for Xenon (a.) and Krypton (b.) at a Discharge Voltage of 500 V

Electron temperature mapping for the 500 V cases are shown in Fig. 20. There is a region of high electron temperature that begins immediately upstream of the acceleration zone and continues into the acceleration zone. This region is similar in dimension and magnitude for both propellants, although in the krypton case the acceleration zone starts slightly farther downstream. The maximum electron temperature of both xenon and krypton cases reaches approximately 50 eV, although there is one "hot" spot in the krypton case that reaches 60 eV. It is important to note that the least robust aspect of this study is the electron temperature calculation. For this reason, the maximum electron temperature for the xenon and krypton cases are considered effectively equal. Also, more conclusive trends in electron temperature trends are best determined with Langmuir probe measurements, which will be conducted at a later date. There is also an additional region of high electron temperature near the anode, which is comparable in magnitude to the "hot" region near the acceleration zone. The source of this anode heating is not clear, but this behavior is also observed by Meezan et al.[12] It could be the case that the emissive probe enters a different regime of

operation that increases the error in the electron temperature calculation method. The existence of this near anode heating will be studied at a later date with single Langmuir probe measurements.

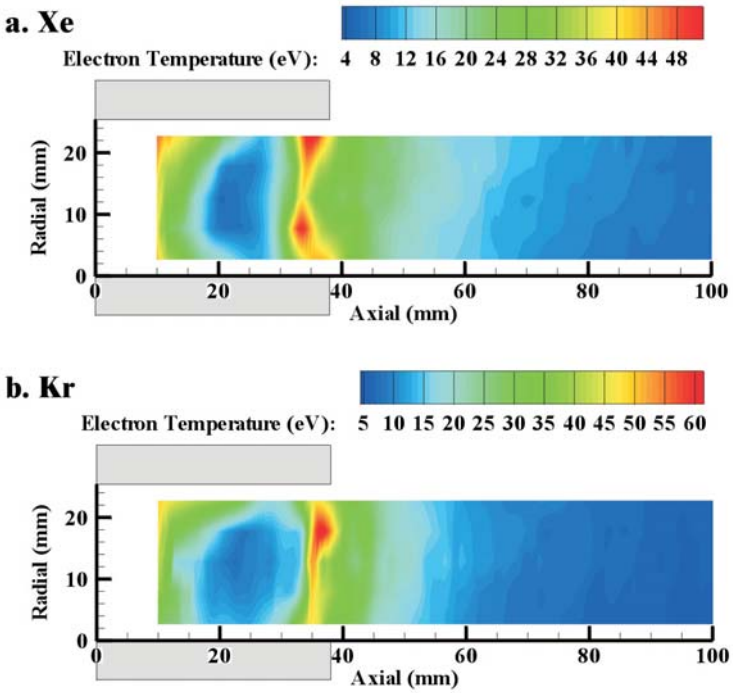

Figure 10. Electron Temperature Map for Xenon (a.) and Krypton (b.) at a Discharge Voltage of 500 V

The axial electric fields are shown in Fig. 11. In this figure, it is possible to see the longer acceleration zone in the krypton case. For xenon, the maximum electric field reaches approximately 70 V/mm. For krypton, the maximum axial electric field is also approximately 70 V/mm, but extends over only a thin region in the acceleration zone. Figure 11 also shows that there is a potential well downstream of the main acceleration zone. This can be seen as a dark spot in the middle of the mapped area between the axial locations of 40-45 mm. This potential well has also been observed by Haas[11], Hofer[38] and Raitses.[15]

Radial electric fields can be seen in Fig. 12. Xenon's beam focusing and krypton's defocusing are well illustrated by the compression and expansion points near the channel walls and exit. The maximum radial electric fields are approximately 20% of the maximum axial electric field for both xenon and krypton. The xenon focusing occurs just

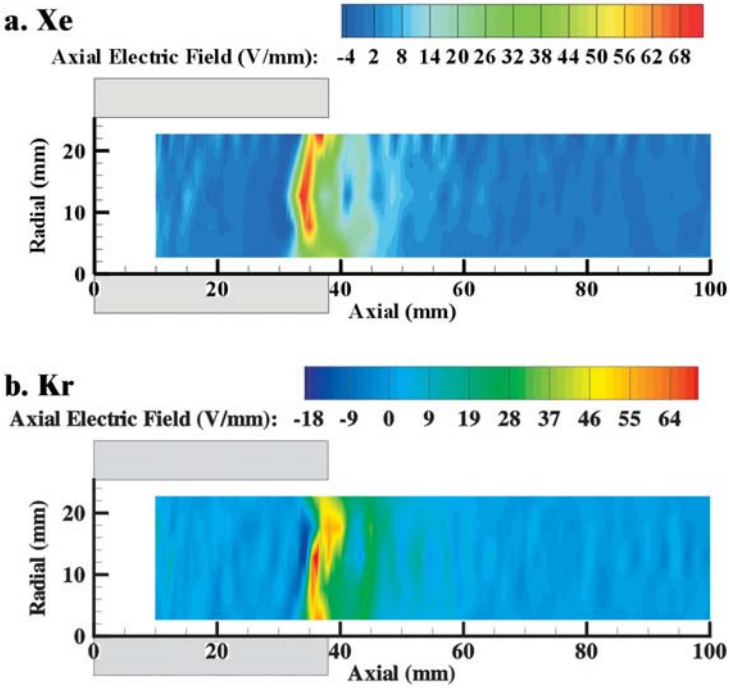

Figure 11. Axial Electric Field Map for Xenon (a.) and Krypton (b.) at a Discharge Voltage of 500 V

inside the discharge channel, but the krypton defocusing occurs just downstream of the exit. This means that there probably would not be increased wall losses due to an unusually high number of krypton ion-wall collisions.

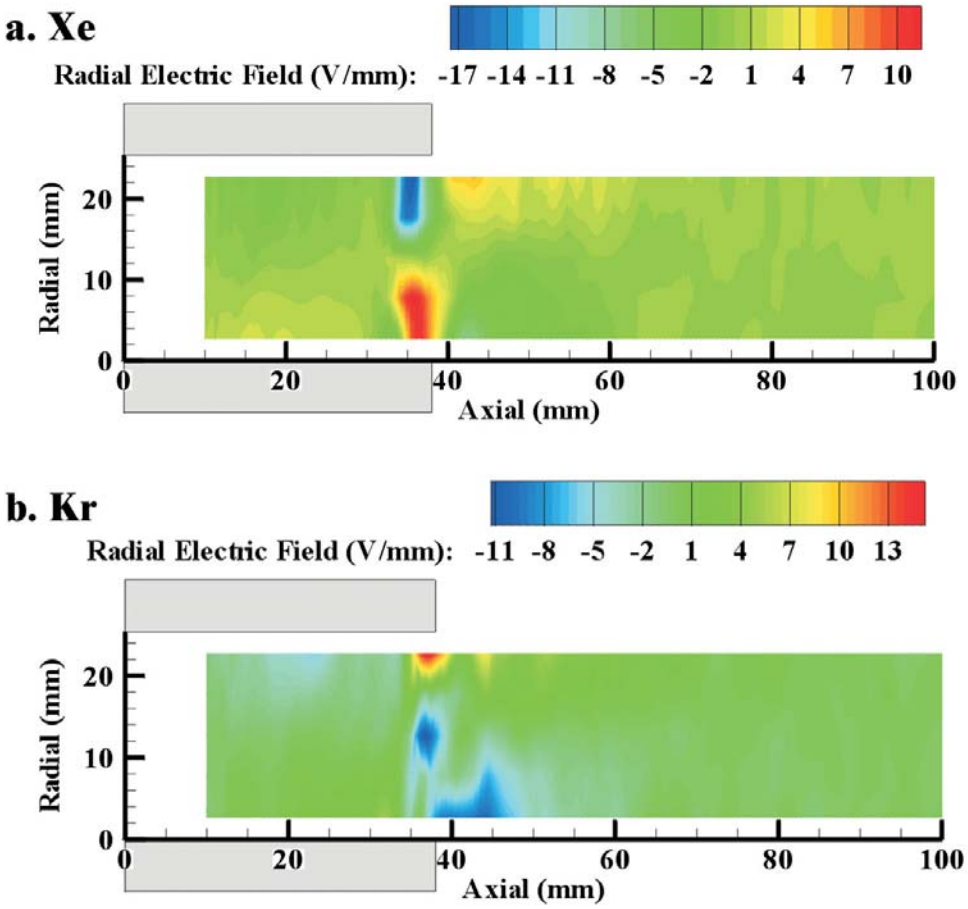

Figure 12. Radial Electric Field Map for Xenon (a.) and Krypton (b.) at a Discharge Voltage of 500 V

B. 600 V Comparison

As in the 500 V case, the 600 V data show a remarkable correspondence between the magnetic pathlines and the equipotential lines (Fig. 13). Again, this correlation between equipotential lines and magnetic field pathlines results in strong focusing for the xenon case and defocusing in the krypton case. Interestingly, the 600 V case also shows a weak "plasma jet" behavior, which has also been observed by Haas.[11] This behavior is visible in the area downstream of the main acceleration zone where the magnetic field pathlines are slightly convex.

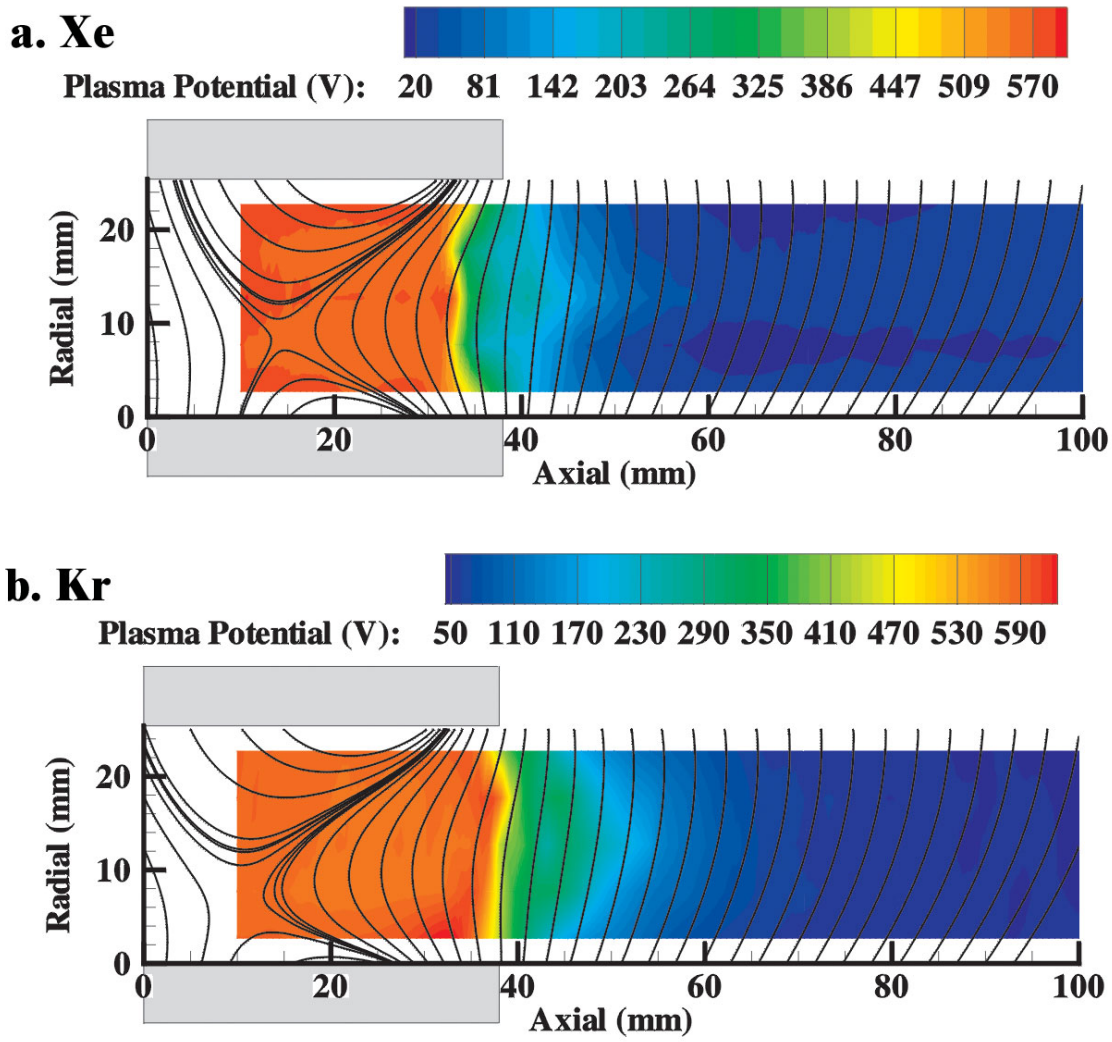

Figure 13. Plasma Potential Map for Xenon (a.) and Krypton (b.) at a Discharge Voltage of 600 V

Figure 14 shows the electron temperature map for the 600 V cases. The same high electron temperature regimes exist in the 600 V case as in the 500 V case, although the anode heating zone is not captured in the 600 V krypton data. In the xenon case, the maximum electron temperature is about 47 eV. In the krypton case, the maximum electron temperature is between 50 and 60 eV in most of the discharge channel, although there is a "hot spot" on the inner discharge channel wall that reaches 85 eV. The high electron temperature regions are similar in dimension for the xenon and krypton cases although the krypton case is located slightly farther downstream.

The maximum electron temperatures are similar in the 600 V and the 500 V cases. This result is expected since the electron temperature is anticipated to saturate near 50-60 eV due to discharge channel wall losses.[13,14,39,40] Since wall losses are the driving factor in determining electron temperature, it is not surprising that the xenon and krypton cases saturate at approximately the same electron temperature.

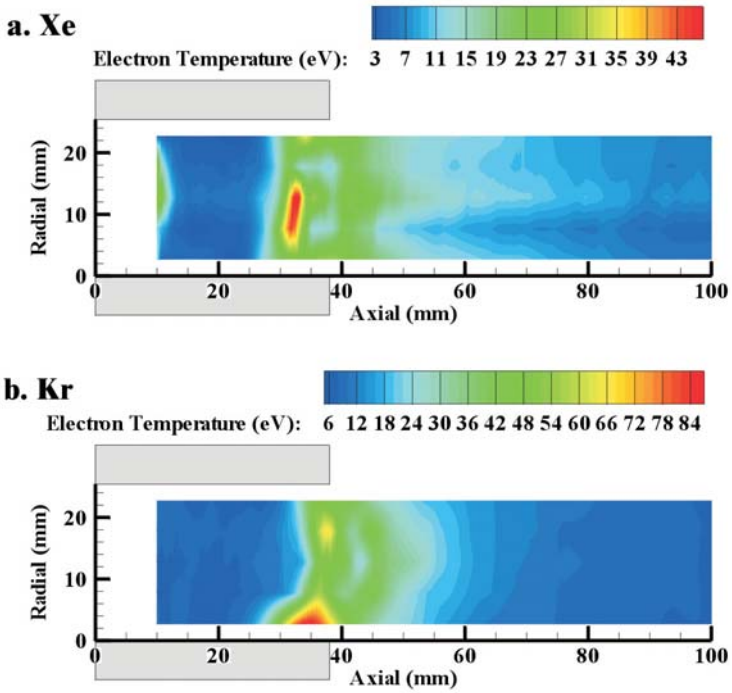

Figure 14. Electron Temperature Map for Xenon (a.) and Krypton (b.) at a Discharge Voltage of 600 V

The axial and radial electric fields are shown in Figs. 15 and 16, respectively. Figure 15 illustrates that krypton's acceleration zone is longer and located farther downstream than the xenon case. The maximum axial electric fields are 150 V/mm and 115 V/mm in the xenon and krypton cases, respectively. Also visible in Fig. 15 is the potential well located between the axial locations of 40 and 45 mm.

The radial electric fields shown in Fig. 16 demonstrate the strong focusing and defocusing seen in the xenon and krypton cases, respectively. The maxim radial electric field is 36 V/mm for the xenon case and 28 V/mm in the krypton case, which is greater than 20% of the maximum axial electric field. The maximum radial electric field is just upstream of the discharge channel exit in the xenon case and begins at the exit for the krypton case. As in the 500 V case, this suggests that there would be no unexpectedly high wall losses due to this krypton defocusing.

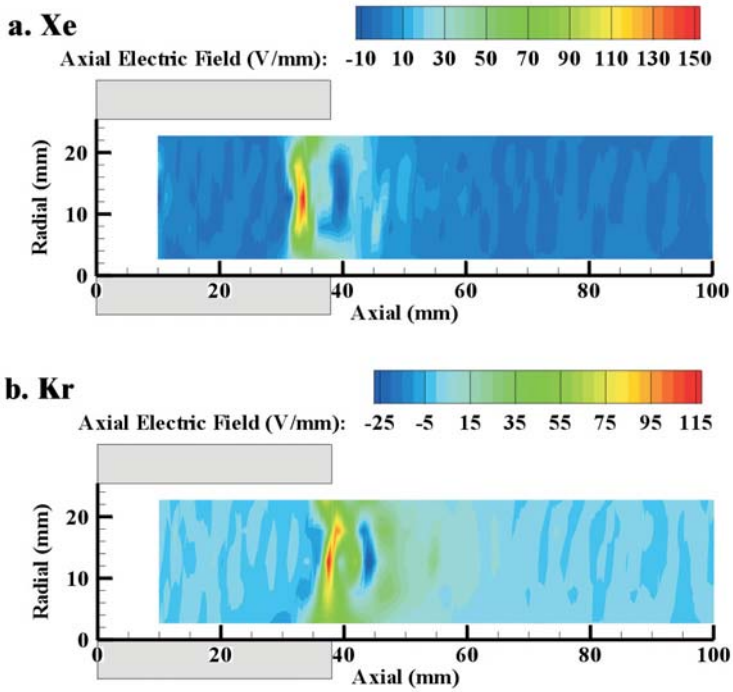

Figure 15. Axial Electric Field Map for Xenon (a.) and Krypton (b.) at a Discharge Voltage of 600 V

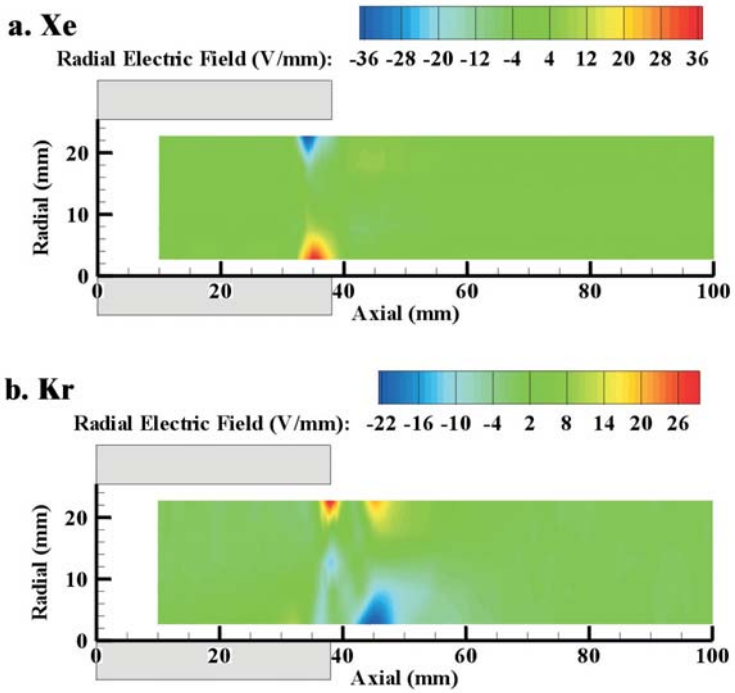

Figure 16. Radial Electric Field Map for Xenon (a.) and Krypton (b.) at a Discharge Voltage of 600 V

C. Acceleration Zone Dimensions

For the operation points given in Table 1, the average acceleration zone start, end, lengths, and the amount of the acceleration zone located outside the thruster are given in Table 2. The acceleration zone start is defined to be the point at which the 90% of the potential drop remains; the acceleration zone end is the point at which the 10% of the acceleration drop remains. The average is calculated by taking the mean of the 5 radial probe sweeps. The krypton acceleration zone begins between 1.7 and 4.6 mm farther downstream than the corresponding xenon points for the 500 and 600 V cases, respectively. Also, the krypton acceleration length is 1.9 and 7.1 mm longer for krypton in the 500 and 600 V cases, respectively. Although both xenon and krypton have a significant portion of their acceleration zone located outside the discharge channel, krypton's acceleration zone extends much farther than xenon's. Since the krypton acceleration zone starts farther downstream, is longer in length, and is almost entirely located outside of the discharge channel, it is not surprising that krypton has a larger beam divergence than xenon.[6,10] The krypton ions that are accelerated away from the discharge channel centerline will have less chance to collide with the channel wall and therefore will accelerate freely to high angles off thruster centerline.

Table 2. Acceleration Zone Dimensions

Point #	Propellant	V_d, V	Avg. Length, mm	Avg. Start, mm	Avg. End, mm	% Outside Thruster
1	Xenon	500	17.3	33.8	51.2	76.0
2	Xenon	600	15.1	32.4	47.5	62.8
3	Krypton	500	19.9	35.5	55.4	87.6
4	Krypton	600	22.2	37.0	59.2	95.4

The dispersion efficiency characterizes the effect of the spread in ion velocities in the Hall thruster plume and is given by the equation: $\eta_d = \langle v_a \rangle^2 / \langle v_a^2 \rangle$. In this equation, v_a represents the ion velocity. With a longer acceleration length, one might expect krypton to have lower dispersion efficiency than xenon. However, retarding potential analyzer measurements indicate that krypton actually has a smaller spread in ion velocity than xenon cases.[10] Since ion velocity dispersion is dictated by the ionization zone, this indicates that the majority of the krypton ionization must be occurring upstream of the acceleration zone. Unfortunately, further studies will have to be conducted to study this behavior in detail (e.g. Langmuir probe measurements).

The start and end of the acceleration zones for the 500 and 600 V cases can be seen in Fig. 17. This figure illustrates krypton's longer acceleration length and that a large percentage of the acceleration zone appears outside of the discharge channel. Roughly speaking, the acceleration zone for krypton begins only slight farther downstream than the corresponding xenon cases.

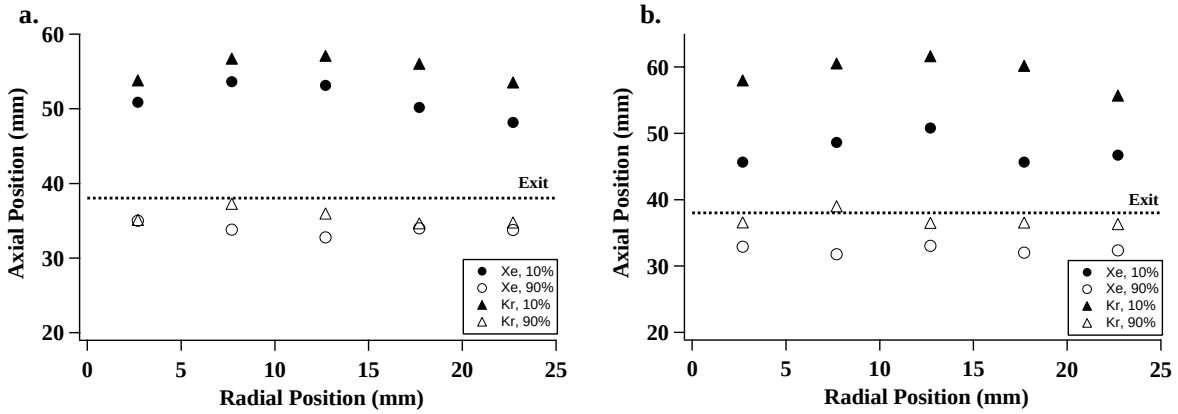

Figure 17. Acceleration Length for Xenon and Krypton at a Discharge Voltage of 500 V (a.) and a Discharge Voltage of 600 V (b.)

IV. Conclusion

The internal plasma structure inside the NASA-173Mv1 has been successfully mapped for xenon and krypton operation. The plasma potential profile is shown to be well correlated with the magnetic field pathlines. In the xenon cases the ions are focused toward the center of the discharge channel and in the krypton cases the ions are defocused. The maximum radial electric field in all of the xenon and krypton cases is equal to or greater than 20% of the maximum axial electric field. In addition, the acceleration zone is found to be longer and located further downstream for the krypton cases. These trends act to defocus the krypton ions and explain the larger beam divergence that is an important contributing factor to the xenon-krypton efficiency gap.

Both propellants have high electron temperature regions that are similar in length and electron temperature. The high electron temperature region near the acceleration zone is located slightly farther downstream in the krypton cases. The maximum electron temperature is approximately 50-60 eV for krypton and xenon at both 500 and 600 V.

The defocusing of the ions is attributed to krypton's magnetic field topology, which is optimized for krypton at a much different magnetic field topology than that corresponding to xenon. Krypton optimization is centrally focused on propellant utilization optimization and for this reason other efficiency components (such as beam divergence) suffer. There is a complicated coupling between beam divergence and propellant utilization that should be a focus of future study. This raises the question, of what can be done to design a krypton Hall thruster to optimize for both propellant utilization and ion beam focusing.

Acknowledgments

We would like to thank the Association Francois-Xavier Bagnoud for their financial support during Mr. Jesse Linnell's graduate studies and NASA Glenn Research Center for financial support through research grant NCC04GA38G (grant monitor Mr. David Jacobson).

References

[1]Kim, V., "Main Physical Features and Processes Determining the Performance of Stationary Plasma Thrusters," Journal of Propulsion and Power, Vol. 14, No. 5, 1998, pp. 736-746, September-October 1998.

[2]Zhurin, V. V., Kaufman, H. R., Robinson, R. S., "Physics of Closed Drift Thrusters," Plasma Sources Science and Technology, Vol. 8, No. 1, 1999, pp. R1-R20, February 1999.

[3]Marrese, C., Haas, J. M., Domonkos, M. T., Gallimore, A. D., Tverdokhlebov, S., Garner, C. E., "The D-100 Performance and Plume Characterization of Krypton," *32nd AIAA/ASME/SAE/ASEE Joint Propulsion Conference*, AIAA-96-2969, Lake Buena Vista, FL, July 1-3, 1996.

[4]Kim, V., Popov, G., Kozlov, V., Skrylnikov, A., Grdlichko, D., "Investigation of SPT Performance and Particularities of its Operation with Krypton and Xenon Mixtures," *27th International Electric Propulsion Conference*, 065, Pasadena, CA, October, 2001.
[5]Semenkin, A. V., Gorshkov, G. O., "Study of Anode Layer Thruster Operation with Gas Mixtures," *24th International Electric Propulsion Conference*, September 1995.
[6]Bugrova, A. I., Lipatov, A. S., Morozov, A. I., Solomatina, L. V., "Global Characteristics of an ATON Stationary Plasma Thruster Operating with Krypton and Xenon," Plasma Physics Reports, Vol. 28, No. 12, 2002, pp. 1032-1037, 2002.
[7]Bugrova, A. I., Lipatov, A. S., Morozov, A. I., Churbanov, D. V., "On a Similarity Criterion for Plasma Accelerators of the Stationary Plasma Thruster Type," Technical Physics Letters, Vol. 28, No. 10, 2002, pp. 821-823, October 2002.
[8]Jacobson, D. T., Manzella, D. H., "50 KW Class Krypton Hall Thruster Performance," *39th Joint Propulsion Conference*, Huntsville, AL, July 20-23, 2003.
[9]Peterson, P. Y., Jacobson, D. T., Manzella, D. H., John, J. W., "The Performance and Wear Characterization of a High-Power High-Isp NASA Hall Thruster," *41st AIAA/ASME/SAE/ASEE Joint Propulsion Conference*, 2005-4243, Tucson, Arizona, 10-13 July 2005.
[10]Linnell, J. A., Gallimore, A. D., "Efficiency Analysis of a Hall Thruster Operating with Krypton and Xenon," *41st AIAA/ASME/SAE/ASEE Joint Propulsion Conference*, AIAA-2005-3683, Tucson, Arizona, July 10-13, 2005.
[11]Haas, J. M., Gallimore, A. D., "Internal Plasma Potential Profiles in a Laboratory-Model Hall Thruster," Physics of Plasmas, Vol. 8, No. 2, 2001, pp. 652-660, February 2001.
[12]Meezan, N. B., Hargus, W. A., Cappelli, M. A., "Anomalous Electron Mobility in a Coaxial Hall Discharge Plasma," Physical Review E, Vol. 63, No. 026410, 2001, January 24, 2001.
[13]Raitses, Y., Staack, D., Smirnov, A., Fisch, N. J., "Space Charge Saturated Sheath Regime and Electron Temperature Saturation in Hall Thrusters," Physics of Plasmas, Vol. 12, 2005, 7 July 2005.
[14]Raitses, Y., Staack, D., Keidar, M., Fisch, N. J., "Electron-Wall Interaction in Hall Thrusters," Physics of Plasmas, Vol. 12, 2005, 2 May 2005.
[15]Raitses, Y., Staack, D., Dorf, L., Fisch, N. J., "Experimental Study of Acceleration Region in a 2 kW Hall Thruster," *39th Joint Propulsion Conference*, 2003-5153, Huntsville, Alabama,
[16]Staack, D., Raitses, Y., Fisch, N. J., "Temperature Gradient in Hall Thrusters," Applied Physics Letters, Vol. 84, No. 16, 2004, pp. 3028-3030, April 2004.
[17]Linnell, J. A., Gallimore, A. D., "Internal Plasma Structure Measurements of a Hall Thruster Using Plasma Lens Focusing," *41st AIAA/ASME/SAE/ASEE Joint Propulsion Conference*, AIAA-2005-4402, Tucson, Arizona, July 10-13, 2005.
[18]Dushman, S., *Scientific Foundations of Vacuum Technique*, Vol. 4, Wiley, New York, 1958, Pages.
[19]Lide, D. R., *CRC Handbook of Chemistry and Physics*, 73rd Edition Ed., CRC Press, Boca Raton, Ann Arbor, London, Tokyo, 1992, Pages.
[20]Dymond, J. H., Smith, E. B., *The Virial Coefficients of Pure Gases and Mixtures, a Critical Compilation*, Oxford University Press, New York, 1980, Pages.
[21]Hofer, R. R., "Development and Characterization of High-Efficiency, High-Specific Impulse Xenon Hall Thrusters," Doctoral Thesis, Dept. of Aerospace Engineering, University of Michigan, Ann Arbor, MI, 2004.
[22]Hofer, R. R., Gallimore, A. D., "The Role of Magnetic Field Topography in Improving the Performance of High-Voltage Hall Thrusters," *38th Joint Propulsion Conference*, Indianapolis, IN, July 7-10, 2002.
[23]Gavryshin, V. M., Kim, V., Kozlov, V. I., Maslennikov, N. A., "Physical and Technical Bases of the Modern SPT Development," *24th International Electric Propulsion Conference*, Moscow, Russia, Sept 19-23, 1995.
[24]Morozov, A. I., "Focusing of Cold Quasineutral Beams in Electromagnetic Fields," Soviet Physics - Doklady, Vol. 10, No. 8, 1966, pp. 775-777, February, 1966.
[25]Bugrova, A. I., Morozov, A. I., Popkov, G. B., Kharchevnikov, V. K., "Characteristics of a Plasma Lens," Soviet Physics. Technical Physics, Vol. 31, No. 2, 1986,
[26]Morozov, A. I., Esinchuk, Y. V., Tilinin, G. N., Trofimov, A. V., Sharov, Y. A., Shchepkin, G. Y., "Plasma Acceleration with Closed Electron Drift and Extended Acceleration Zone," Soviet Physics - Technical Physics, Vol. 17, No. 1, 1972, pp. 38-45, July, 1972.
[27]Haas, J. M., "Low-perturbation Interrogation of the Internal and Near-field Plasma Structure of a Hall Thruster Using a High-Speed Probe Positioning System," Thesis, Dept. of Aerospace Engineering, University of Michigan, 2001.
[28]Haas, J. M., Gallimore, A. D., McFall, K., Spanjers, G., "Development of a High-Speed, Reciprocating Electrostatic Probe System for Hall Thruster Interrogation," Review of Scientific Instruments, Vol. 71, No. 11, 2000, pp. 4131-4138, November 2000.
[29]Hershkowitz, N., Cho, M. H., "Measurement of Plasma Potential Using Collecting and Emitting Probes," Journal of Vacuum Science and Technology A, Vol. 6, No. 3, 1988, pp. 2054-2059, May/June 1988.
[30]Staack, D., Raitses, Y., Fisch, N. J., "Sheilded Electrostatic Probe for Nonperturbing Plasma Measurements in Hall Thruster," Review of Scientific Instruments, Vol. 75, No. 2, 2004, pp. 393-399, February 2004.
[31]Dorf, L., Raitses, Y., Fisch, N. J., "Electrostatic Probe Apparatus for Measurements in the Near-Anode Region of Hall Thrusters," Review of Scientific Instruments, Vol. 75, No. 5, 2004, pp. 1255-1260, May 2004.
[32]Reinsche, C. H., "Smoothing by Spline Functions," Numerische Mathematik, Vol. 10, 1967, pp. 177-183, 1967.

[33]Hobbs, G. D., Wesson, J. A., "Heat Flow Through a Langmuir Sheath in the Presence of Electron Emission," Plasma Physics, Vol. 9, 1967, pp. 85-87, 1967.
[34]Intrator, T., Cho, M. H., Wang, E. Y., Hershkowitz, N., Diebold, D., DeKock, J., "The Virtual Cathode as a Transient Double Sheath," Journal of Applied Physics, Vol. 64, No. 6, 1988, pp. 2927-2933, 1988.
[35]Schwager, L. A., "Effects of Secondary and Thermionic Electron Emission on the Collector and Source Sheaths of a Finite Ion Temperature Plasma Using Kinetic Theory and Numerical Simulation," Physics of Fluids B: Plasma Physics, Vol. 5, No. 2, 1993, pp. 631-645, 1993.
[36]Keidar, M., Boyd, I. D., Beilis, I. I., "Plasma Flow in Plasma-Wall Transition in Hall Thruster Channel," Physics of Plasmas, Vol. 8, No. 12, 2001, pp. 5315-5322, December 2001.
[37]Keidar, M., Boyd, I. D., "On the Magnetic Mirror Effects in Hall Thrusters," Applied Physics Letters, Vol. 87, No. 121501, 2005, August 1, 2005.
[38]Hofer, R. R., Gallimore, A. D., "Recent Results from Internal and Very-Near-Field Plasma Diagnostics of a High Specific Impulse Hall Thruster," *28th International Electric Propulsion Conference*, Toulouse, France, March 17-21, 2003.
[39]Ahedo, E., Escobar, D., "Influence of Design and Operation Parameters on Hall Thruster Performances," Journal of Applied Physics, Vol. 96, No. 2, 2004, pp. 983-992, July 2004.
[40]Barral, S., Makowski, K., Peradzyski, Z., Gascon, N., Dudeck, M., "Wall Material Effects in Stationary Plasma Thrusters. II. Near-Wall and In-Wall Conductivity," Physics of Plasmas, Vol. 10, No. 10, 2003, pp. 4137-4152, October 2003.